



Cite this: *RSC Adv.*, 2025, 15, 4562

# Studying CeO<sub>2</sub>-modified defective carbon as an electrocatalyst for electrochemical reduction of CO<sub>2</sub>†

Yihan Wu, Ying Chang\* and Jingchun Jia \*

The electrochemical CO<sub>2</sub> reduction reaction (CO<sub>2</sub>RR) is regarded as an efficient approach to obtain high value-added chemicals and fuels. It can store intermittent renewable energy and enable artificial carbon cycling. However, on account of the small number of active sites in traditional carbon materials, the electrocatalytic performance is poor. Meanwhile, rare earth elements play a significant role in many fields owing to their abundant electronic energy levels, attracting increasing attention from the scientific community. In this study, we modified defective carbon with cerium oxide (CeO<sub>2</sub>) to produce abundant oxygen vacancies, and the synthesized V<sub>0</sub>-CeO<sub>2</sub>-1300 catalyst showed excellent catalytic performance for generating CO. At a low potential of −0.8 V (vs. RHE), the Faraday efficacy for CO could reach 79.65%. The current density was 12.6 mA cm<sup>−2</sup> at −1.4 V. It was experimentally proved that loading cerium atoms on defective carbon is vital for promoting the catalytic performance of the CO<sub>2</sub>RR, endorsing the use of rare earth catalysts in electrochemical reactions at room temperature.

Received 18th December 2024

Accepted 28th January 2025

DOI: 10.1039/d4ra08845j

rsc.li/rsc-advances

## 1. Introduction

Carbon dioxide (CO<sub>2</sub>) is a common odorless greenhouse gas. Greenhouse gases keep the earth warm by preventing the escape of heat from the earth's surface into space. However, in recent decades, the overuse of fossil fuels has not only given rise to a serious energy dilemma but also led to significant CO<sub>2</sub> emissions, resulting in severe environmental problems.<sup>1,2</sup> Large emissions of CO<sub>2</sub> have also had destructive impacts on the daily lives of people. To rationally solve these problems, people have put forward the strategy of “carbon peak” and “carbon neutrality”, and the proposal of the dual-carbon goal marks a new understanding of CO<sub>2</sub> emissions.<sup>3</sup> CO<sub>2</sub> is also an economical and renewable carbon resource.<sup>4,5</sup> Using renewable energy to reduce CO<sub>2</sub> to renewable fuels or valuable chemicals is not only conducive to alleviating the environmental problems caused by excessive CO<sub>2</sub> emissions but also enables the use of CO<sub>2</sub>. At the same time, it can alleviate the energy crisis and reduce dependence on fossil fuels.<sup>6–8</sup> In the CO<sub>2</sub>RR, energy is stored in the form of chemical bonds, which provides a viable method for the conversion of renewable electric energy sources into high value-added fuels and chemical feedstocks. In the CO<sub>2</sub>RR, the conversion of CO<sub>2</sub> into CO is technically and

economically feasible because of its low input, high product yield, and good selectivity. CO can yield a variety of fuels because it can be used as a chemical raw material; therefore, the CO<sub>2</sub>RR is considered one of the most promising reactions in the chemical industry.<sup>9</sup> Moreover, using a suitable electrocatalyst, the double electron transfer product CO can be generated with low overpotential and high Faraday efficiency.<sup>10</sup> However, there is competition from the hydrogen evolution reaction (HER) in the catalytic process because both carbon dioxide and protons (H<sup>+</sup>) need to participate in the CO<sub>2</sub>RR, and in many cases, the thermodynamic HER competes with the CO<sub>2</sub>RR for protons and electrons.<sup>11</sup> Therefore, it is a great challenge to develop catalysts with high activity, selectivity and stability.<sup>12</sup>

It is well known that electrocatalysts can lower the activation energy barrier for the reaction, thereby increasing the reaction rate.<sup>13</sup> Traditional electrocatalysts mainly comprise precious metals like Ag, Au, Pd, and Ir. However, due to their relative scarcity and high cost, they cannot be applied on a large scale. Therefore, at the forefront of the research field, researchers have favored the development, design and synthesis of some low-cost and high-performance electrocatalysts. It has been reported that carbon-based catalysts can be used as potential substitutes for CO<sub>2</sub>RR precious metal catalysts. Among them, one-dimensional carbon materials have the advantages of a high exposed surface atomic percentage, large specific surface area and low price compared with traditional catalytic materials.<sup>14,15</sup> Therefore, it is of immense use in the area of electrocatalysis. Moreover, some nanoparticles help improve the catalytic activity.<sup>16</sup> Some electrochemical reactions, such as the CO<sub>2</sub>RR and HER, are sensitive to the size and morphology of

College of Chemistry and Environmental Science, Inner Mongolia Key Laboratory of Green Catalysis and Inner Mongolia Collaborative Innovation Center for Water Environment Safety, Inner Mongolia Normal University, Hohhot, 010022, China. E-mail: changying@imnu.edu.cn; jjc1983@126.com

† Electronic supplementary information (ESI) available. See DOI: <https://doi.org/10.1039/d4ra08845j>



nanoparticle catalysts, which affect their product selectivity.<sup>17</sup> In general, introducing heteroatoms such as N on the surface of carbon-based catalysts leads to defective carbon, which improves the activity of carbon-based catalysts and modifies their surface chemical properties.<sup>18,19</sup> When the carbon material of the substrate is doped, it can furnish a higher specific surface area and thus better contact with the CO<sub>2</sub> in the electrolyte.<sup>20</sup>

Rare earth (RE) is a general term for scandium, yttrium, and lanthanide of Group IIIB of the periodic table. Generally, the typical chemical valence state of rare earth elements is trivalent, but in electrochemical reduction, rare earth elements can be quickly converted into different valence states, promoting charge transfer and specific absorption of intermediates.<sup>21,22</sup> Rare earths have many 4f orbitals with higher energy levels. Due to the relatively weak shielding effect of the rare earth 4f electrons, it can interact strongly with external electrons, thus exhibiting unique chemical and electronic properties.<sup>23–25</sup> Rare earth-based materials also reveal good liveness in some catalytic processes, such as CO<sub>2</sub>RR, electrocatalytic N<sub>2</sub> reduction reaction (NRR), and oxygen reduction reaction (ORR). Rare earth oxides such as CeO<sub>2</sub> are usually not considered candidates for electrochemical research due to their low conductivity and high dielectric constant.<sup>26</sup> CeO<sub>2</sub> can generate strong metal-carrier interactions due to its abundant oxygen vacancy defects and unique electronic structure, which may help enhance the thermal stability of the catalyst in certain thermocatalytic reactions, thereby improving its catalytic activity.<sup>27</sup> CeO<sub>2</sub> has high water activation liveness in the CO<sub>2</sub> hydrogenation reaction but reveals poor activity in the HER.<sup>28</sup> Moreover, Ce can take advantage of the uniqueness of the electron arrangement on the f orbital to form redox ion pairs, which is beneficial to the adsorption and activation of CO<sub>2</sub> in the CO<sub>2</sub>RR process.<sup>29,30</sup> CeO<sub>2</sub> has been applied as a cocatalyst to promote conversion in various electrochemical reactions.<sup>31</sup>

In this study, the oxygen vacancies on the surface of cerium can enhance the adsorption of CO<sub>2</sub>, and the defect sites introduced in the high-temperature pyrolysis carbon material are used to form a composite catalyst to improve the performance of CO<sub>2</sub>RR. In this study, nitrogen-doped carbon CO<sub>2</sub>RR catalysts supported by Ce were synthesized in a simple pyrolysis method, and the proportion of rare earth metals and pyrolysis temperature were systematically adjusted to study their influences on catalytic performance. The introduction of Ce regulates the electronic structure of the electrocatalyst by optimizing the composition to ensure improved electron transfer while inhibiting the HER.<sup>32</sup> When the pyrolysis temperature is 1300 °C and the content of Ce is 0.2 mmol, the CO<sub>2</sub> reduction performance of the catalyst is the best, and the maximum Faraday efficiency of Ce generation is 79.65% at a potential of −0.8 V, and the current density is 12.6 mA cm<sup>−2</sup> at −1.4 V. After 12 hours of stability test, there was no significant change in current density and FE<sub>CO</sub>. The surface catalyst has good stability.

## 2. Experiment

### 2.1 Chemicals

Cerium nitrate hexahydrate (Ce(NO<sub>3</sub>)<sub>3</sub>·6H<sub>2</sub>O, 99.99%) (Shanghai Titan Technology Co., LTD), dicyandiamine (C<sub>2</sub>H<sub>4</sub>N<sub>4</sub>,

>98%) (Sinopharm Chemical Reagent Co., LTD), glucose (C<sub>6</sub>H<sub>12</sub>O<sub>6</sub>, >99.7%) (Tianjin Fuchen Chemical Reagent Co., LTD), potassium bicarbonate (KHCO<sub>3</sub>, 97%) (Sinopharm Chemical Reagent Co., LTD). The catalyst ink was made using Nafion solution (10 wt%, D-520).

### 2.2 Synthesis of materials

The inexpensive, environmentally friendly graphite-phase carbon nitride template (g-C<sub>3</sub>N<sub>4</sub>) is readily pyrolyzed from nitrogen-doped precursors such as dicyandiamine (DCA). Carbon nitride is an ideal template for trapping and fixing a high load of monatoms and clusters.<sup>33,34</sup> As shown in Fig. 1a, the catalyst is prepared by the self-sacrificing template method of g-C<sub>3</sub>N<sub>4</sub>.<sup>35</sup> Firstly, glucose, DCA and a certain amount of Ce(NO<sub>3</sub>)<sub>3</sub>·6H<sub>2</sub>O were fully stirred and mixed at indoor temperature to yield the precursor and then placed in the freeze-dryer to dry the sample using the solid-gas phase transformation of the substance. Subsequently, the resulting sample was annealed in argon. In the low-temperature pyrolysis process (550 °C), DCA polycondensates into layered g-C<sub>3</sub>N<sub>4</sub> and constructs a provisional layer template that limits the polymerization of carbon intermediates and maintains a uniform distribution of Ce-containing precursors. After annealing at higher temperatures (1300 °C), the g-C<sub>3</sub>N<sub>4</sub> template acts as a sacrificial template and a nitrogen-rich polymer, completing decomposition and releasing much of the carbonized gas. In this process, a porous carbon structure with sufficient defect sites and nitrogen doping is generated to help stabilize Ce. At the same time, the carbon intermediate is carbonized to form a conductive carbon skeleton, and the Ce nanoparticles are dispersed on the defective carbon. We named the prepared catalyst V<sub>0</sub>-CeO<sub>2</sub>/C-1300 and the Ce-free catalyst V<sub>0</sub>-C-1300. For researching the influence of the Ce content in the catalyst on electrocatalytic activity, a series of samples were prepared at 1300 °C by changing the initial amount of Ce. The contents of Ce were 0.1 mmol, 0.2 mmol and 0.4 mmol, respectively. To study the effect of temperature on the electrocatalytic activity of the catalyst, a series of catalysts with a Ce content of 0.2 mmol and without Ce were prepared at different pyrolysis temperatures (800 °C to 1400 °C) for comparative experiments.

### 2.3 Physical characteristics

The structure, morphology and content distribution of the catalysts were obtained by scanning electron microscopy (SEM) of ZEISS sigma500 and transmission electron microscopy (TEM) of JEOL-JEM 2100F. The crystal structure of the catalyst was obtained through Bruker D8 Advance X-ray powder diffractometer (XRD). X-ray photoelectron spectroscopy (XPS) tests were carried out by Thermo Scientific ESCALAB to determine the sample composition and elemental valence state of the catalyst. Raman tests were performed by Horiba scientific-LabRAM HR Evolution in Japan to determine the defect density and graphitization degree in the catalyst. The superficial area and aperture distribution of the catalyst were determined using US-McASAP2460. The X-ray absorption spectra (XAS) of the samples were collected at the Beijing Synchronous Light

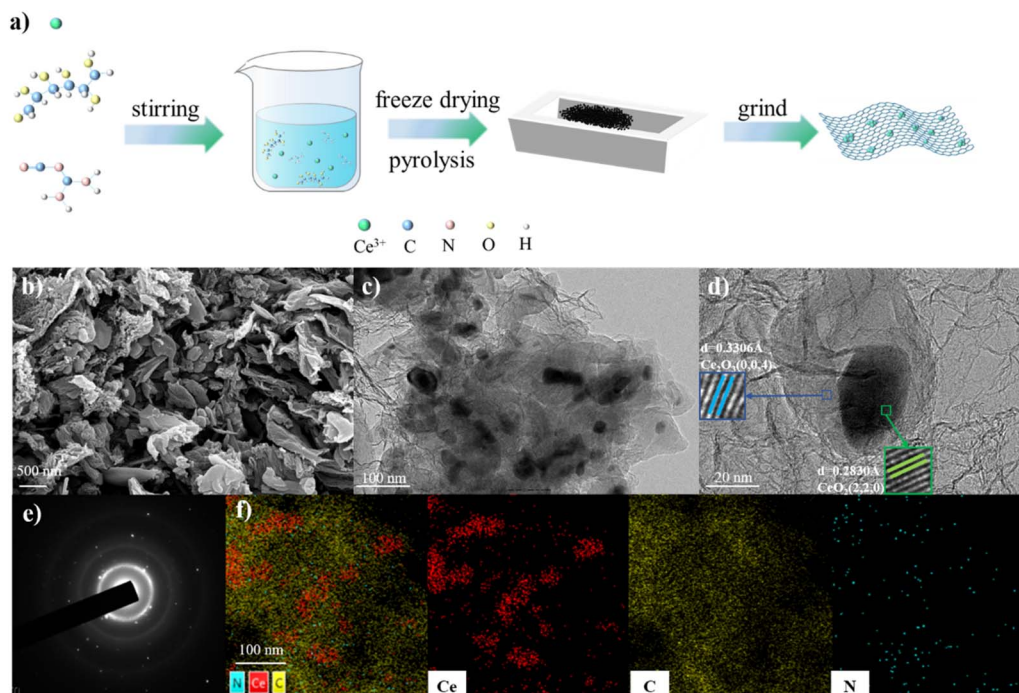


Fig. 1 (a) Schematic of the synthesis of  $V_0\text{-CeO}_2/\text{C-1300}$ . (b) SEM image, (c–e) TEM image, and (f) EDS elemental mappings of  $V_0\text{-CeO}_2/\text{C-1300}$ .

Source (SSLS) Center using  $\text{CeO}_2$  and  $\text{CeCl}_3$  as the reference of Ce  $L_3$ -edge (5723 eV). The extended edge X-ray absorption fine structure (EXAFS) was obtained by Fourier transform fitting of X-ray absorption near-side structure (XANES).

## 2.4 Electrochemical test

Specifically,  $\text{CO}_2\text{RR}$  is an electrolytic process of reducing  $\text{CO}_2$  to the target product using electricity. This experiment is to test the catalytic property of  $\text{CO}_2$  reduction in a three-electrode H-type electrolytic cell. The electrochemical reduction of  $\text{CO}_2$  occurs in a batch mode.<sup>36</sup>  $\text{CO}_2\text{RR}$  occurs at the solid–liquid two-phase interface where the working electrode in an H-cell electrolyzer touches the electrolyte. The three-electrode H-type electrolytic cell is mainly divided into three parts: cathode chamber, anode chamber and ion exchange membrane.<sup>37</sup> The two cells are separated by a Nafion membrane.  $\text{CO}_2\text{RR}$  occurs in the cathode chamber, where a minor side reaction of  $\text{H}^+$  electrochemical reduction to  $\text{H}_2$  occurs. The OER occurs in the anode chamber, which is located on the other side of the battery. As an isolation layer between the cathode chamber and the anode chamber, the ion exchange membrane can selectively allow ions to exchange from both sides of the electrolytic chamber, isolate the electrolyte in the electrolytic chamber, and prevent the direct flow of ions. The main part of the H-type electrolytic cell also includes a working electrode, a reference electrode and a counter-electrode.<sup>38</sup> A solid  $\text{Ag}/\text{AgCl}$  electrode is the reference electrode, Pt electrode is the counter electrode and carbon paper coated with catalyst is the working electrode. 10 mL 0.5 M  $\text{KHCO}_3$  solution served as the electrolyte. Nafion,  $\text{H}_2\text{O}$  and  $\text{C}_2\text{H}_5\text{OH}$  were placed in a container in a ratio of 1 : 9 :

10 and ultrasonically treated for more than 30 min to make a Nafion solution with a concentration of 25%. The temperature was 25 °C and the pressure was standard atmospheric pressure. The catalyst paste was prepared by ultrasonically dispersing  $V_0\text{-CeO}_2/\text{C-1300}$  in diluted Nafion solution at a 1 : 10 ratio. The working electrode was made by evenly applying 70  $\mu\text{L}$  slurry twice in the 1 cm  $\times$  1 cm area of the 1 cm  $\times$  2 cm carbon paper and drying it in the air or infrared light.

The cathode cell is purged with carbon dioxide for more than 30 minutes before the test to form a saturated  $\text{CO}_2$  solution, which is continued throughout the test. In electrochemical testing, the cyclic voltammetry (CV) test (−0.8 V to −1.8 V) is first performed to make a steady state. The beginning potential of  $\text{CO}_2\text{RR}$  was measured by linear sweep voltammetry (LSV) in the range of −0.8 V and −1.8 V. Chronoamperometry ( $i$ – $t$ ) is performed at a defined potential and connected to a gas chromatograph for online testing. Gas chromatography (GC method, use Agilent 7890B) was used to detect CO and  $\text{H}_2$  in the product through a thermal conductivity detector (TCD) and hydrogen flame ionization detector (FID). The following potential is converted to the potential at a relative criterion reversible hydrogen electrode by the equation  $E_{\text{RHE}} = E$  (vs. RHE) + 0.6.

## 3. Results and discussion

The preparation process of  $V_0\text{-CeO}_2/\text{C-1300}$  is shown in Fig. 1a. First, quantitative glucose, DCA and  $\text{Ce}(\text{NO}_3)_3 \cdot 6\text{H}_2\text{O}$  were thoroughly stirred to form the precursor, and then the resulting mixture was freeze-dried for 24 hours to obtain a white





flocculent sample. The obtained sample was placed in a porcelain boat and then pyrolyzed in a tubular furnace in two steps. During the 550 °C pyrolysis process, DCA is condensed into layers of g-C<sub>3</sub>N<sub>4</sub>, creating a provisional layer template and limiting the polymerization of carbon intermediates. After annealing at high temperatures (1300 °C), the g-C<sub>3</sub>N<sub>4</sub> template acts as a sacrificial template and a nitrogen-rich polymer, completing the decomposition and releasing the carbonized gas. This produces a porous carbon structure with many sites and nitrogen doping.

The scanning electron microscopy images in Fig. 1b and S1 (ESI)<sup>†</sup> show that all the samples were composed of folded nanosheets. This is due to the shape of the soft template g-C<sub>3</sub>N<sub>4</sub>; more folds can have a larger active area, and the surface of the sample is rougher after the addition of cerium and the surface is uneven. The V<sub>0</sub>-CeO<sub>2</sub>/C-1300 sample was analyzed using TEM, and carbon structure with abundant pores can be clearly observed (Fig. 1c and S2<sup>†</sup>). This structure can heighten mass transfer in electrochemical processes while exposing more defect sites.<sup>39,40</sup> The rare earth cerium aggregates on the graphene layer, forming nanoparticles of different sizes. High-temperature calcination causes metal migration, forming metal nanoclusters during the synthesis process. The dashed fringes obtained by HRTEM images are shown in Fig. 1d, and

the lattice spacing of nanoparticles is 0.2830 nm and 0.3306 nm, matching with the (220) crystal surface of CeO<sub>2</sub> and the (004) crystal surface of Ce<sub>2</sub>O<sub>3</sub>, indicating the formation of Ce oxides. As shown in Fig. 1f, energy dispersive X-ray spectroscopy (EDS) confirms the presence of C, N, and Ce elements in V<sub>0</sub>-CeO<sub>2</sub>/C-1300. Table S1<sup>†</sup> shows the element contents of C, N and Ce. Confirming the TEM results, rare earth Ce shows a certain amount of aggregation. Notably, the presence of Ce nanoparticle aggregation in the TEM image is similar to that shown in the SAED pattern with Ce diffraction spots (Fig. 1e). Several halos have been observed in the SAED patterns, proving that it is a typical polycrystalline structure.

Further characterization of V<sub>0</sub>-CeO<sub>2</sub>/C-1300 and V<sub>0</sub>-C-1300 samples by XRD, as shown in Fig. 2a and S5,<sup>†</sup> shows that all of the samples contain a wide peak in the crystal plane of graphite (JCPDS no. 26-1077) (005), showing these catalysts all have a graphite structure.<sup>41</sup> In addition, the (005) diffraction peak has a negative shift relative to the standard graphite ( $\approx 26.6^\circ$ ) at  $\approx 25.9^\circ$ , indicating that nitrogen doping leads to a larger interlayer distance, which is conducive to mass transfer in electrochemical reactions.<sup>42,43</sup> The catalyst prepared at a low pyrolysis temperature did not show an obvious peak containing Ce, which may be due to the low crystallinity of Ce in V<sub>0</sub>-CeO<sub>2</sub>/C (Fig. S4<sup>†</sup>). The peaks of cerium oxides, the peaks of CeO<sub>2</sub> (JCPDS

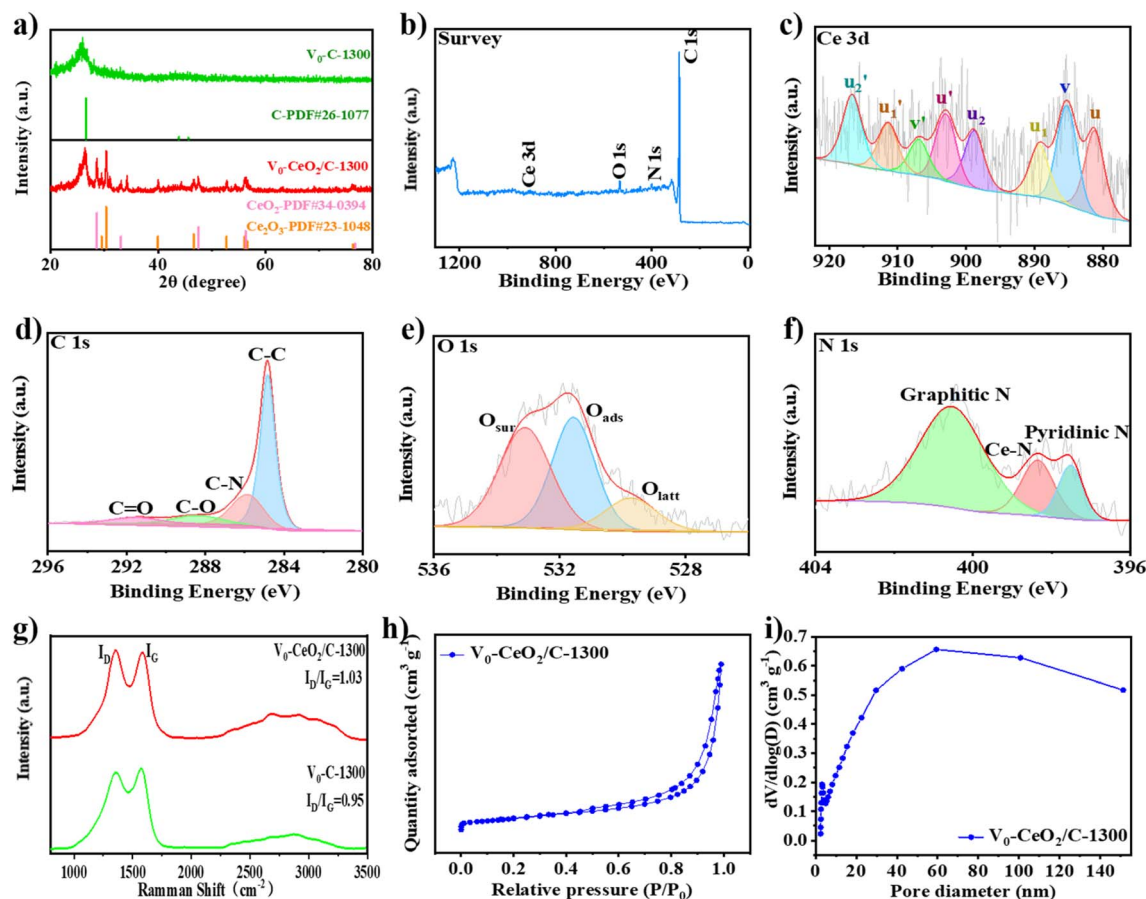


Fig. 2 (a) XRD patterns. XPS spectra of V<sub>0</sub>-CeO<sub>2</sub>/C-1300: (b) survey spectrum, (c) Ce 3d spectrum, (d) C 1s spectrum, (e) O 1s spectrum and (f) N 1s spectrum. (g) Raman spectrum, (h) N<sub>2</sub> adsorption/desorption isotherms and (i) pore size distribution.



no. 34-0394) (005) crystal plane and the peaks of  $\text{Ce}_2\text{O}_3$  (JCPDS no. 23-1048) (101) crystal plane in the sample can be detected from the XRD when the temperature rises and the crystallinity is higher.

We studied the chemical composition and valence states of  $\text{V}_0\text{-CeO}_2/\text{C-1300}$  and  $\text{V}_0\text{-C-1300}$  samples through XPS. Fig. 2b is an XPS full-light image. The catalyst contains C, N, O, Ce elements. Fig. 2c shows the Ce XPS spectrum of the prepared  $\text{V}_0\text{-CeO}_2/\text{C-1300}$  catalyst. The composite spectrum of Ce 3d consists of 8 independent peaks, whose distribution is shown in Fig. 2c. Peaks labeled  $u'$ ,  $u'_1$ ,  $u'_2$  and  $u$ ,  $u_1$ ,  $u_2$  belong to Ce  $3d_{5/2}$  and Ce  $3d_{3/2}$  orbits, respectively, and are the characteristic peaks of  $\text{Ce}^{4+}$ .<sup>44</sup> The largest BE peaks,  $u'_2$  (917.4 eV) and  $u_2$  (899.6 eV) occur in the Ce ( $3d^9 4f^0$ ) O ( $2p^6$ ) final state. The low BE states  $u'_1$  (912.2 eV) and  $u_1$  (890.1 eV) are assigned to Ce ( $3d^9 4f^1$ ) O ( $2p^5$ ). The BE peaks for  $u'$  (903.7 eV) and  $u$  (881.9 eV) correspond to the Ce ( $3d^9 4f^2$ ) O ( $2p^4$ ) final state.<sup>45</sup> Peaks labeled  $v'$  and  $v$  at 907.7 eV and 886.1 eV are the characteristic peaks of  $\text{Ce}^{3+}$ .<sup>46</sup> The ratio of  $\text{Ce}^{3+}/(\text{Ce}^{3+} + \text{Ce}^{4+})$  in the catalyst can be calculated by the peak area and the corresponding components in the XPS spectrum, which usually reflects the  $\text{V}_0$  content of the catalyst and the  $\text{V}_0$  content in  $\text{V}_0\text{-CeO}_2/\text{C-1300}$  is 29%.<sup>47</sup>

The C 1s spectrum demonstrates the existence of C-N groups, showing that N was doped into the carbon during the annealing process (Fig. 2d). The O 1s spectrum is divided into  $\text{O}_{\text{surf}}$  (533.9 eV) for surface adsorption of  $\text{H}_2\text{O}$ ,  $\text{O}_{\text{ads}}$  (532.3 eV) for surface adsorption of oxygen, and  $\text{O}_{\text{latt}}$  (530.5 eV) for bonding with metal lattice oxygen. The relative content of  $\text{O}_{\text{ads}}$  is closely related to the oxygen vacancy because the dissociated molecular oxygen is adsorbed on the surface oxygen vacancy. The relative content of  $\text{O}_{\text{ads}}$  in  $\text{V}_0\text{-CeO}_2/\text{C-1300}$  is increased compared to that in  $\text{V}_0\text{-C-1300}$  (*i.e.*, 51.5% *versus* 50.7%) (Fig. 2e and S6<sup>†</sup>), indicating that the introduction of  $\text{CeO}_2$  does contribute to the enrichment of oxygen vacancies. High-temperature pyrolysis in an anaerobic environment can cause  $\text{CeO}_2$  nanoparticles to produce oxygen vacancies. The N 1s spectrum of  $\text{V}_0\text{-CeO}_2/\text{C-1300}$  and  $\text{V}_0\text{-C-1300}$  samples show two types of nitrogen, including pyridine N and graphite N (Fig. 2f). The nitrogen of  $\text{V}_0\text{-CeO}_2/\text{C-1300}$  and  $\text{V}_0\text{-C-1300}$  is mainly pyridine nitrogen and graphite nitrogen, which can improve the starting potential, limit the current density, accelerate the electron transfer path, and thus improve the  $\text{CO}_2\text{RR}$  performance.<sup>48–50</sup> In particular, the proportion of pyridine N in  $\text{V}_0\text{-CeO}_2/\text{C-1300}$  increased significantly compared to that of  $\text{V}_0\text{-C-1300}$  (Fig. S6<sup>†</sup>), showing that a high content of pyridine nitrogen is beneficial to  $\text{CO}_2$  reduction reaction (*i.e.*, 18.9% *versus* 16.8%).<sup>51–53</sup> This is because the presence of Ce leads to more defect sites, which promotes a higher ratio of pyridine nitrogen.<sup>54</sup>

Fig. 2g shows the Raman spectra of  $\text{V}_0\text{-CeO}_2/\text{C-1300}$  and  $\text{V}_0\text{-C-1300}$  samples, where two characteristic peaks are observed at  $\approx 1353\text{ cm}^{-1}$  (D band) and  $\approx 1583\text{ cm}^{-1}$  (G band). The other three Raman peaks of 2D, D + G and 2D' are also observed in the sample. All the observed modes are resonant, except that the G mode is single resonance, and the rest are double resonances.<sup>55</sup> When the annealing temperature increased from 900 °C to 1100 °C, the G peak increased from  $1533.27\text{ cm}^{-1}$  to  $1563.04\text{ cm}^{-1}$ . When  $T = 1300\text{ °C}$ , the G peak rises to

$1581.99\text{ cm}^{-1}$ , and the upward shift may be due to the decrease in N atom content.<sup>56</sup> It is worth noting that the  $I_{\text{D}}/I_{\text{G}}$  peak intensity ratio (1.02 to 1.04) of the  $\text{V}_0\text{-CeO}_2/\text{C}$  sample (Fig. S7<sup>†</sup>) is higher than that of the  $\text{V}_0\text{-C-1300}$  sample (0.95), reflecting the existence of many defects in  $\text{V}_0\text{-CeO}_2/\text{C-1300}$ , which is better for improving electrocatalytic activity. In order to measure the specific surface area and pore structure, nitrogen adsorption/desorption tests were performed on a series of  $\text{V}_0\text{-CeO}_2/\text{C-1300}$  and  $\text{V}_0\text{-C-1300}$  (Fig. S8<sup>†</sup>) samples. As shown in Fig. 2h,  $\text{V}_0\text{-CeO}_2/\text{C-1300}$  shows a type II isotherm and a high surface area of around  $149.6\text{ m}^2\text{ g}^{-1}$ . The corresponding curve aperture distribution is shown in Fig. 2i and S8<sup>†</sup>, indicating the  $\text{V}_0\text{-CeO}_2/\text{C-1300}$  sample has a layered microscopic-macro pore structure. Possibly due to the release of much nitrogen-containing gas during the annealing process, this porous structure exists in  $\text{V}_0\text{-CeO}_2/\text{C-1300}$ . The pore size of the rare earth-free sample is significantly smaller than that of the rare earth-containing sample, indicating that the temperature is too high. The structure will collapse, affecting the gas passage, and some active sites are covered, but Ce can protect the structure, which is conducive to the diffusion and migration of  $\text{CO}_2$  molecules.<sup>57,58</sup>

In order to further understand the valence coordination environment of Ce in  $\text{V}_0\text{-CeO}_2/\text{C-1300}$ , XANES and EXAFS were characterized. As shown in Fig. 3a,  $\text{CeO}_2$  has two weak characteristic peaks at 5731.8 eV and 5738.5 eV due to the superposition of two final states of Ce ( $2p^4 f^{0.5} d^*$  and  $2p^4 f^{1.5} d^*$ , L, L represents L in the ligand).  $\text{CeCl}_3$  has a strong characteristic peak at 5725.9 eV, corresponding to electron excitation from the  $\text{Ce}^{3+}$  core  $2p_{3/2}$  state to the local 5d state ( $2p^4 f^{1.5} d^*$ ).<sup>59</sup> For  $\text{V}_0\text{-CeO}_2/\text{C-1300}$ , two peaks are observed at 5730.9 eV and 5738.4 eV, respectively, indicating that the electronic configuration of  $\text{V}_0\text{-CeO}_2/\text{C-1300}$  is similar to that of  $\text{Ce}^{4+}$ . The near edge adsorption of  $\text{V}_0\text{-CeO}_2/\text{C-1300}$  is located between  $\text{CeCl}_3$  and  $\text{CeO}_2$  but closer to  $\text{CeO}_2$ , indicating that the valence state of Ce in  $\text{V}_0\text{-CeO}_2/\text{C-1300}$  is mainly +4, which is conducive to the formation of oxygen vacancies.<sup>60</sup> We studied the local coordination environment of Ce in  $\text{V}_0\text{-CeO}_2/\text{C-1300}$  through FT of EXAFS. As shown in Fig. 3b,  $\text{V}_0\text{-CeO}_2/\text{C-1300}$  has only one wide peak at  $1.75\text{ Å}$ , indicating the presence of Ce–O coordination. The EXAFS spectra of  $\text{V}_0\text{-CeO}_2/\text{C-1300}$  show that the coordination number of Ce–O is 6 (Table S2<sup>†</sup>). Compared with  $\text{CeO}_2$ ,  $\text{V}_0\text{-CeO}_2/\text{C-1300}$ , with more O vacancies, has a lower coordination number (*i.e.*, 6 *versus* 8).<sup>61</sup> The wavelet transform diagram (Fig. 3c) shows that the maximum intensity of  $\text{V}_0\text{-CeO}_2/\text{C-1300}$  in  $K$ -space ( $3.3\text{ Å}^{-1}$ ) is different from that of  $\text{CeCl}_3$  ( $4.4\text{ Å}^{-1}$ ) but very close to that of  $\text{CeO}_2$  ( $3.9\text{ Å}^{-1}$ ), further indicating the presence of Ce–O bonds.<sup>62,63</sup>

Based on the above results, it can be proved that Ce oxides exist in  $\text{V}_0\text{-CeO}_2/\text{C-1300}$ . When  $\text{Ce}^{3+}$  is converted to  $\text{Ce}^{4+}$ , it will be accompanied by the generation of oxygen vacancies. Because the radius of  $\text{Ce}^{3+}$  is larger than that of  $\text{Ce}^{4+}$ , lattice expansion occurs during the reduction process, which will generate oxygen vacancies. The adsorption and activation of  $\text{CO}_2$  molecules are considered an important step in the conversion of  $\text{CO}_2$  to CO. It has been reported that oxygen vacancies can be used to promote the adsorption of  $\text{CO}_2$ . In addition, oxygen vacancies can also



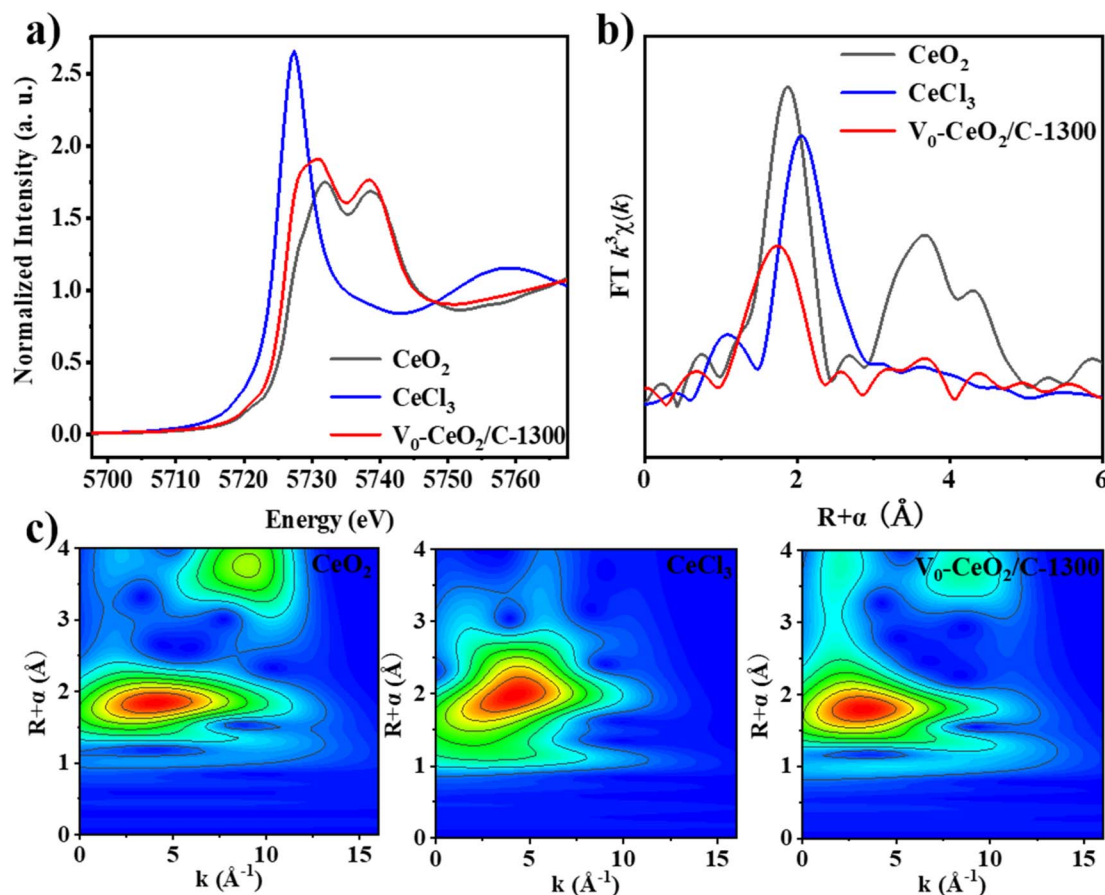


Fig. 3 (a) Normalized Ce L<sub>3</sub>-edge XANES spectra of V<sub>0</sub>-CeO<sub>2</sub>/C-1300, (b) FT k<sub>3</sub>-weighted Ce L<sub>3</sub>-edge EXAFS spectra of V<sub>0</sub>-CeO<sub>2</sub>/C-1300 and the references, and (c) wavelet transform EXAFS of V<sub>0</sub>-CeO<sub>2</sub>/C-1300.

reduce the energy barrier of the rate-determining step (from \*COOH to \*CO), thereby increasing the activity and selectivity of CO<sub>2</sub>RR to CO.<sup>64</sup> From a thermodynamic point of view, the adsorption and strength of CO<sub>2</sub> on the material surface are the key to reducing the energy barrier of CO<sub>2</sub> conversion.<sup>65</sup> Oxygen vacancies enhance the adsorption capacity and bonding strength of the catalyst to CO<sub>2</sub>, which helps reduce the thermodynamic energy barrier of CO<sub>2</sub>RR and improve its electrocatalytic carbon dioxide reduction performance.<sup>66</sup> Therefore, the valence transition of Ce can produce abundant oxygen vacancy defects, and the presence of Ce oxides enables the reduction of CO<sub>2</sub> to CO.<sup>67–69</sup>

It is generally believed that rare earth nanoscale oxides have no catalytic activity for room-temperature electrochemistry.<sup>70</sup> To determine whether it has CO<sub>2</sub>RR performance, we first measured the linear sweep voltammetry curves of V<sub>0</sub>-CeO<sub>2</sub>/C-1300 in CO<sub>2</sub> and Ar gas-saturated electrolytes over an identical voltage range (Fig. 4a and S9†). It can be seen from the figure that the current density of V<sub>0</sub>-CeO<sub>2</sub>/C-1300 in the Ar-saturated electrolyte is lower than that in the CO<sub>2</sub>-saturated electrolyte, which preliminarily indicates that V<sub>0</sub>-CeO<sub>2</sub>/C-1300 has excellent CO<sub>2</sub>RR performance. Notably, as shown in Fig. 4a, V<sub>0</sub>-CeO<sub>2</sub>/C-1300 has a significantly higher current density than V<sub>0</sub>-C-1300 over the same voltage range, indicating that V<sub>0</sub>-CeO<sub>2</sub>/C-

1300 would exhibit better CO<sub>2</sub>RR activity than V<sub>0</sub>-C-1300. This result further confirms that rare earth-modified defective carbon catalysts often exhibit better catalytic performance than catalysts without rare earth modification. However, the initial potential and current density of several samples synthesized at different temperatures show negligible differences. In order to better compare the activity and selectivity of the samples prepared at different temperatures, the performance of the catalyst was tested in an H-type electrolytic cell.

Subsequently, the CO<sub>2</sub>RR performance of V<sub>0</sub>-CeO<sub>2</sub>/C-1300 was evaluated by the *i*-*t* method in 0.5 M KHCO<sub>3</sub> electrolyte at indoor temperature and atmospheric pressure in an H-type cell. The gas outcomes were quantitatively tested by gas chromatography. Only H<sub>2</sub> and CO gas outcomes were found in the test voltage range, but no liquid outcomes. In the same tested voltage range (Fig. 4b), V<sub>0</sub>-CeO<sub>2</sub>/C-1300 exhibits high CO selectivity at −0.8 V, with a Faraday efficiency of up to 79.65%, and maintains a Faraday efficiency of more than 70% over a wide voltage window (−0.7 V to −1.0 V). In contrast, at 1300 °C, the highest Faraday efficiency without Ce is only 26.84%. These conclusions show that the distribution of Ce element on the carrier is the reason for the significant improvement of CO<sub>2</sub>RR performance. Compared to the catalyst with the same Ce content at 1300 °C, the effect of nanocrystals formed at other



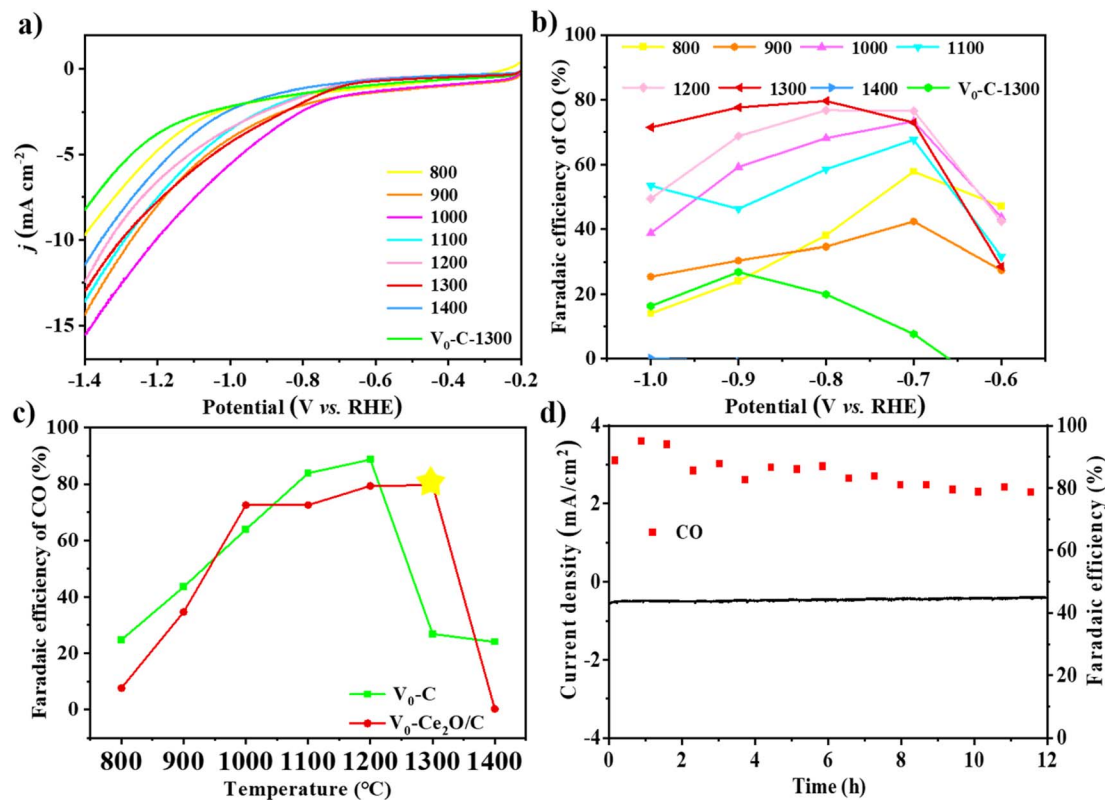


Fig. 4 (a and b) LSV curves and  $FE_{CO}$  of  $V_0-CeO_2/C$  at different temperatures and  $V_0-C-1300$ . (c)  $FE_{CO}$  of  $V_0-CeO_2/C$  and  $V_0-C$  at different temperatures. (d) Stability test at  $-0.80$  V of  $V_0-CeO_2/C-1300$ .

temperatures is poor. At  $800$  °C and  $1400$  °C, the Faraday efficiency of  $V_0-CeO_2/C$  is less than 20%. Compared with  $V_0-CeO_2/C$  at different temperatures, the catalyst showed higher selectivity for CO at  $1300$  °C, which may be due to its large specific surface area and high defect content, forming more catalytic active sites. Comparison with other catalysts containing rare earth elements (Table S3†), the product is the catalytic performance of CO, and the catalytic performance of this study belongs to the medium level. This is also consistent with the LSV curve results. In the temperature range of  $800$  °C to  $1400$  °C, the FE variation of  $V_0-C$  and  $V_0-CeO_2/C$  showed a volcanic trend, as shown in Fig. 4c. When the temperature is low, the active sites containing defective carbon may promote the reaction of carbon dioxide. The presence of heteroatoms destroys the integrity of the  $\pi$  connection of the carbon plane, and in turn, optimizes the charge state of adjacent carbon atoms, making them potential active sites.<sup>71,72</sup> However, when the temperature reaches  $1300$  °C, the defective carbon structure may collapse, and the presence of Ce can keep the carbon skeleton stable so that the active sites are fully exposed. Moreover, cerium oxide can produce a large number of oxygen vacancy defects, which further promotes the electrochemical reduction of  $CO_2$  so that the performance of  $V_0-CeO_2/C-1300$  is nearly 4 times higher than that of  $V_0-C-1300$ . To evaluate the stability of  $V_0-CeO_2/C-1300$ , constant-potential electrolysis was performed at  $-0.8$  V for 12 hours. Fig. 4d shows that the attenuation of the  $V_0-CeO_2/C-1300$  current density is almost

negligible after 12 hours of electrolysis, while the CO Faraday efficiency remains above 79%. This result shows that  $V_0-CeO_2/C-1300$  has excellent stability. According to Fig. S10,† we find that after 12 hours of durability test, the flocculent structure of the carbon material still exists, but the diameter is smaller. At the same time, the particle size of cerium oxide also decreased. However, the overall morphology of the catalyst did not change significantly.<sup>73</sup> We also evaluated the effects of different weight ratios of  $V_0-CeO_2/C-1300$  on electrocatalytic  $CO_2$  reduction (Fig. S11†). When the content of Ce in  $V_0-CeO_2/C-1300$  is  $0.2$  mmol, the potential is  $-0.8$  V, and the CO yield of the catalyst is the highest. When the Ce content is  $0.1$  mmol, a lower rare earth content leads to fewer oxygen vacancies, which is not conducive to the adsorption of  $CO_2$ . When the Ce content is  $0.4$  mmol, Ce aggregates on the C template and the nanoparticles accumulate on the active sites, reducing the active surface area.  $V_0-CeO_2/C-1300$ , with a  $0.2$  mol content of Ce, was the most suitable for catalyzing  $CO_2$ RR. In summary, when the content of Ce is  $0.2$  mmol and the temperature is  $1300$  °C, the synergistic effect of carbon and Ce is the best for the electrochemical reduction of  $CO_2$  to CO, with the inhibition of the hydrogen evolution reaction.

The Electrochemical Active Surface Area (ECSA) describes the intrinsic activity of a catalyst. We measured the double-layer capacitance ( $C_{dl}$ ) of the material by cyclic voltammetry and further calculated the electrochemical active area of the material. As shown in Fig. S12,† the active area of all samples is not



very different. This shows that the effect of temperature on the active area is not very large. We also performed electrochemical impedance tests for  $V_0$ -CeO<sub>2</sub>/C at different temperatures and for  $V_0$ -C-1300 (Fig. S13†). The electrochemical impedance reflects the transmission capacity of electrons, and the low impedance value indicates that it has low electron transmission resistance. Cerium oxides use 4f electrons to demonstrate superior electron transport, thereby reducing the energy barrier and accelerating the electron movement in the electrocatalytic reaction sequence.<sup>74</sup> The smallest semicircle radius shows that  $V_0$ -CeO<sub>2</sub>/C-1300 has the smallest charge transfer resistance, which is more conducive to CO<sub>2</sub>RR. In summary, using high pyrolysis temperature to form intrinsic defects and Ce to stabilize the porous carbon structure and produce abundant oxygen vacancies is an effective strategy to promote CO<sub>2</sub>RR.

The satisfactory electrocatalytic performance of  $V_0$ -CeO<sub>2</sub>/C-1300 can be attributed to (1) intrinsic carbon defects can be used as independent non-metallic active sites in electrocatalytic reactions due to the redistribution of electrons in the surrounding defects. (2) The rare earth metal Ce is used to modify the defective carbon so that the carbon framework still maintains a good structure at high temperatures, which is conducive to the distribution of active sites, thereby improving the catalytic activity of the catalyst. (3) The presence of CeO<sub>2</sub> is beneficial to the formation of oxygen vacancies, enhancing the activation of CO<sub>2</sub> and promoting the electrochemical reduction of CO<sub>2</sub>.<sup>75,76</sup> (4) The mechanism of CO<sub>2</sub> activation by oxygen vacancies mainly includes three steps: adsorption, dissociation and conversion. CO<sub>2</sub> is first adsorbed near the oxygen vacancy, then dissociated, and finally desorbed to obtain the target product CO.<sup>77</sup>

## 4. Conclusion

In summary, we used a simple self-sacrificing template strategy to obtain a Ce nanoparticle-modified defective carbon catalyst. The presence of Ce nanoparticles avoids the collapse of the porous carbon structure at high temperatures, thereby ensuring the exposure of more active sites. The transformation of the Ce valence state can produce abundant oxygen vacancy defects, so the presence of CeO<sub>2</sub> can provide an additional boost for the reduction of CO<sub>2</sub> to CO. The performance of electrochemical reduction of CO<sub>2</sub> is affected by the different metal ratios and pyrolysis temperatures. The optimized  $V_0$ -CeO<sub>2</sub>/C-1300 catalyst has abundant oxygen vacancies, a high density of active sites, and a large pore structure. At -0.8 V potential, the Faraday efficiency is as high as 79%, and it has good durability. This lays a foundation for the further research and development of CO<sub>2</sub>RR catalysts.

## Data availability

Data will be made available on request.

## Conflicts of interest

The authors report no declarations of interest.

## Acknowledgements

We would like to thank the National Natural Science Foundation of China (22362028), the Natural Science Foundation of Inner Mongolia of China (2022QN02002), and the Fundamental Research Funds for the Inner Mongolia Normal University (2022JBBJ011, 2023JBQN047) for financial support.

## References

- 1 B. Jiang, D. Xia, B. Yu, R. Xiong, W. Ao, P. Zhang and L. Cong, An environment-friendly process for limestone calcination with CO<sub>2</sub> looping and recovery, *J. Clean. Prod.*, 2019, **240**, 118147.
- 2 M. D. Porosoff, B. Yan and J. G. Chen, Catalytic reduction of CO<sub>2</sub> by H<sub>2</sub> for synthesis of CO, methanol and hydrocarbons: challenges and opportunities, *Energy Environ. Sci.*, 2016, **9**, 62–73.
- 3 J. Wang, C. Hao, Q. Zhang, Q. Meng and H. Liu, Research advances on photo-assisted CO<sub>2</sub> conversion to methanol, *Appl. Catal., A*, 2022, **643**, 118738.
- 4 S. C. Kang, K.-W. Jun and Y.-J. Lee, Effects of the CO/C-1300 O<sub>2</sub> ratio in synthesis gas on the catalytic behavior in fischer-tropsch synthesis using K/Fe–Cu–Al catalysts, *Energy Fuels*, 2013, **27**, 6377–6387.
- 5 H. D. Matthews, K. Zickfeld, R. Knutti and M. R. Allen, Focus on cumulative emissions, global carbon budgets and the implications for climate mitigation targets, *Environ. Res. Lett.*, 2018, **13**, 010201.
- 6 X. Gao, T. Atchimarungsri, Q. Ma, T.-S. Zhao and N. Tsubaki, Realizing efficient carbon dioxide hydrogenation to liquid hydrocarbons by tandem catalysis design, *J. Energy Chem.*, 2020, **2**, 100038.
- 7 Q. Miao, C. Lu, Q. Xu, S. Yang, M. Liu, S. Liu, C. Yu, X. Zhuang, Z. Jiang and G. Zeng, CoN<sub>2</sub>O<sub>2</sub> sites in carbon nanosheets by template-pyrolysis of COFs for CO<sub>2</sub>RR, *Chem. Eng. J.*, 2022, **450**, 138427.
- 8 M. Aresta, A. Dibenedetto and A. Angelini, Catalysis for the valorization of exhaust carbon: from CO<sub>2</sub> to chemicals, materials, and fuels. technological use of CO<sub>2</sub>, *Chem. Rev.*, 2014, **114**, 1709–1742.
- 9 Y. Jiang, K. Wang, Y. Wang, Z. Liu, X. Gao, J. Zhang, Q. Ma, S. Fan, T.-S. Zhao and M. Yao, Recent advances in thermocatalytic hydrogenation of carbon dioxide to light olefins and liquid fuels via modified fischer-tropsch pathway, *J. CO<sub>2</sub> Util.*, 2023, **67**, 102231.
- 10 Y. Y. Birdja, E. Pérez-Gallent, M. C. Figueiredo, A. J. Göttle, F. Calle-Vallejo and M. T. M. Koper, Advances and challenges in understanding the electrocatalytic conversion of carbon dioxide to fuels, *Nat. Energy*, 2019, **4**, 732–745.
- 11 T. Burdyny and W. A. Smith, CO<sub>2</sub> reduction on gas-diffusion electrodes and why catalytic performance must be assessed at commercially-relevant conditions, *Energy Environ. Sci.*, 2019, **12**, 1442–1453.
- 12 M. Liu, S. Liu, Q. Xu, Q. Miao, S. Yang, S. Hanson, G. Z. Chen, J. He, Z. Jiang and G. Zeng, Dual atomic catalysts from





- COF-derived carbon for CO<sub>2</sub>RR by suppressing HER through synergistic effects, *Carbon Energy*, 2023, 5, e300.
- 13 S. Siahrostami, Designing carbon-based materials for efficient electrochemical reduction of CO<sub>2</sub>, *Ind. Eng. Chem. Res.*, 2018, 58, 879–885.
  - 14 M. H. Jameel, M. Arain, I. Hussain, *et al.*, A review on catalyst convergence: Unleashing the potential of MXenes for CO<sub>2</sub> electrochemical reduction into high-value liquid product, *Nano Mater. Sci.*, 2024, DOI: [10.1016/j.nanoms.2024.06.006](https://doi.org/10.1016/j.nanoms.2024.06.006).
  - 15 Z. Peng, N. Deng, X. Li, H. Chi, H. Wang, W. Kang and B. Cheng, Controllable preparation, working mechanisms, and actual application of various one-dimensional nanomaterials as catalysts for CO<sub>2</sub>RR: a review, *Ind. Eng. Chem. Res.*, 2023, 62, 21511–21535.
  - 16 S. Biswas, Y. Shingyouchi, M. Ogami, *et al.*, Advancing electrochemical CO<sub>2</sub> reduction with group 11 metal nanoclusters for renewable energy solutions, *EcoEnergy*, 2024, 2(3), 400–418.
  - 17 H. Jung, S. Y. Lee, C. W. Lee, M. K. Cho, D. H. Won, C. Kim, H.-S. Oh, B. K. Min and Y. J. Hwang, Electrochemical fragmentation of Cu<sub>2</sub>O nanoparticles enhancing selective C–C coupling from CO<sub>2</sub> reduction reaction, *J. Am. Chem. Soc.*, 2019, 141, 4624–4633.
  - 18 X. Yan, Y. Jia and X. Yao, Defects on carbons for electrocatalytic oxygen reduction, *Chem. Soc. Rev.*, 2018, 47, 7628–7658.
  - 19 R. Kumar, R. K. Singh and R. S. Tiwari, Growth analysis and high-yield synthesis of aligned-stacked branched nitrogen-doped carbon nanotubes using sesame oil as a natural botanical hydrocarbon precursor, *Mater. Des.*, 2016, 94, 166–175.
  - 20 Y. Gang, F. Pan, Y. Fei, Z. Du, Y. H. Hu and Y. Li, Highly efficient nickel, iron, and nitrogen codoped carbon catalysts derived from industrial waste petroleum coke for electrochemical CO<sub>2</sub> reduction, *ACS Sustain. Chem. Eng.*, 2020, 8, 8840–8847.
  - 21 Y. Xue, P. Wang, M. He, T. Zhang, C. Yang and Z. Li, Rare earth nanomaterials in electrochemical reduction of carbon dioxide, *Coord. Chem. Rev.*, 2024, 516, 215983.
  - 22 J. Liu, L. Sun, Y. Sun, J. Sun, Y. Pan, M. Xu, Y. Lang, D. Zhai, W. Deng, Y. Li and L. Yang, Theoretical insights into lanthanide rare earth single-atom catalysts for electrochemical CO<sub>2</sub> reduction, *J. Mater. Chem. A*, 2024, 12, 16183–16189.
  - 23 Z. Zhan, Z. Sun, Z. Wei, Y. Li, W. Chen, S. Li and S. Pang, Atomic interface regulation of rare-earth metal single atom catalysts for energy conversion, *Nano Res.*, 2023, 12, 3493–3515.
  - 24 S. Stojadinović, N. Radić, B. Grbić, S. Maletić, P. Stefanov, A. Pačevski and R. Vasilčić, Structural, photoluminescent and photocatalytic properties of TiO<sub>2</sub>: Eu<sup>3+</sup> coatings formed by plasma electrolytic oxidation, *Appl. Surf. Sci.*, 2016, 370, 218–228.
  - 25 J. Liu, X. Kong, L. Zheng, X. Guo, X. Liu and J. Shui, Rare earth single-atom catalysts for nitrogen and carbon dioxide reduction, *ACS Nano*, 2020, 14, 1093–1101.
  - 26 M. Kumar, J.-H. Yun, V. Bhatt, B. Singh, J. Kim, J.-S. Kim, B. S. Kim and C. Y. Lee, Role of Ce<sup>3+</sup> valence state and surface oxygen vacancies on enhanced electrochemical performance of single step solvothermally synthesized CeO<sub>2</sub> nanoparticles, *Electrochim. Acta*, 2018, 284, 709–720.
  - 27 Z. Liang, L. Yin, H. Yin, Z. Yin and Y. Du, Rare earth element based single-atom catalysts: synthesis, characterization and applications in photo/electro-catalytic reactions, *Nanoscale Horiz.*, 2022, 7, 31–40.
  - 28 X. Yan, C. Chen, Y. Wu, S. Liu, Y. Chen, R. Feng, J. Zhang and B. Han, Efficient electroreduction of CO<sub>2</sub> to C<sub>2+</sub> products on CeO<sub>2</sub>-modified CuO, *Chem. Sci.*, 2021, 12, 6638–6645.
  - 29 Y. Guan, S. Wu, H. Huang, Z. Zhu, W. Tian and A. Yin, Promotion of CO<sub>2</sub> Electroreduction on Bismuth Nanosheets with Cerium Oxide nanoparticles, *Chem.-Asian J.*, 2024, 19(17), e202400296.
  - 30 H. Wang, X. Kang and B. Han, Rare-earth Element-based Electrocatalysts Designed for CO<sub>2</sub> Electro-reduction, *ChemSusChem*, 2024, 17, e202301539.
  - 31 L. Song, Z. Liang, M. Sun, B. Huang and Y. Du, The interfacial effect induced by rare earth oxide in boosting the conversion of CO<sub>2</sub> to formate, *Energy Environ. Sci.*, 2022, 15, 3494–3502.
  - 32 Z. Liang, L. Song, M. Sun, B. Huang and Y. Du, Atomically dispersed indium and cerium sites for selectively electroreduction of CO<sub>2</sub> to formate, *Nano Res.*, 2023, 16, 8757–8764.
  - 33 H. Yu, L. Shang, T. Bian, R. Shi, G. I. N. Waterhouse, Y. Zhao, C. Zhou, L. Z. Wu, C. H. Tung and T. Zhang, Nitrogen-doped porous carbon nanosheets templated from g-C<sub>3</sub>N<sub>4</sub> as metal-free electrocatalysts for efficient oxygen reduction reaction, *Adv. Mater.*, 2016, 28, 5080–5086.
  - 34 Q. Li, D. Xu, X. Ou and F. Yan, Nitrogen-doped graphitic porous carbon nanosheets derived from in situ formed g-C<sub>3</sub>N<sub>4</sub> templates for the oxygen reduction reaction, *Chem.-Asian J.*, 2017, 12, 1816–1823.
  - 35 M. Zhang, H. Li, J. Chen, F. X. Ma, L. Zhen, Z. Wen and C. Y. Xu, High-loading Co single atoms and clusters active sites toward enhanced electrocatalysis of oxygen reduction reaction for high-performance Zn–air battery, *Adv. Funct. Mater.*, 2022, 33, 2209726.
  - 36 H. Rabiee, P. Yan, H. Wang, Z. Zhu and L. Ge, Electrochemical CO<sub>2</sub> reduction integrated with membrane/adsorption-based CO<sub>2</sub> capture in gas-diffusion electrodes and electrolytes, *EcoEnergy*, 2024, 2(1), 3–21.
  - 37 S. Liang, N. Altaf, L. Huang, Y. Gao and Q. Wang, Electrolytic cell design for electrochemical CO<sub>2</sub> reduction, *J. CO<sub>2</sub> Util.*, 2020, 35, 90–105.
  - 38 J. T. Billy and A. C. Co, Experimental parameters influencing hydrocarbon selectivity during the electrochemical conversion of CO<sub>2</sub>, *ACS Catal.*, 2017, 7, 8467–8479.
  - 39 X. Hu, Y. Liu, J. Chen, L. Yi, H. Zhan and Z. Wen, Fast redox kinetics in Bi-heteroatom doped 3d porous carbon nanosheets for high-performance hybrid potassium-ion battery capacitors, *Adv. Energy Mater.*, 2019, 9, 1901533.
  - 40 Y. Cheng, H. Guo, X. Li, X. Wu, X. Xu, L. Zheng and R. Song, Rational design of ultrahigh loading metal single-atoms (Co,



- Ni, Mo) anchored on in-situ pre-crosslinked guar gum derived N-doped carbon aerogel for efficient overall water splitting, *Chem. Eng. J.*, 2021, **410**, 128359.
- 41 G. C. Cheng, G. L. Li, C. D. Liu, L. F. Yuan, W. W. Chen and C. Hao, Efficient synthesis of nitrogen- and sulfur-Co-doped ketjenblack with a single-source precursor for enhancing oxygen reduction reaction activity, *Chemistry*, 2017, **23**, 3674–3682.
  - 42 X. Hu, J. Li, G. Zhong, Y. Liu, J. Yuan, S. Lei, H. Zhan and Z. Wen, Hierarchical multicavity nitrogen-doped carbon nanospheres as efficient polyselenide reservoir for fast and long-life sodium-selenium batteries, *Small*, 2020, **16**, e2005534.
  - 43 X. Hu, G. Zhong, J. Li, Y. Liu, J. Yuan, J. Chen, H. Zhan and Z. Wen, Hierarchical porous carbon nanofibers for compatible anode and cathode of potassium-ion hybrid capacitor, *Energy Environ. Sci.*, 2020, **13**, 2431–2440.
  - 44 G. Zhou, B. Dai, H. Xie, G. Zhang, K. Xiong and X. Zheng, CeCu composite catalyst for CO synthesis by reverse water-gas shift reaction: effect of Ce/Cu mole ratio, *J. CO<sub>2</sub> Util.*, 2017, **21**, 292–301.
  - 45 B. Choudhury, P. Chetri and A. Choudhury, Oxygen defects and formation of Ce<sup>3+</sup> affecting the photocatalytic performance of CeO<sub>2</sub> nanoparticles, *RSC Adv.*, 2014, **4**, 4663–4671.
  - 46 S. Zeng, Y. Wang, S. Ding, J. J. H. B. Sattler, E. Borodina, L. Zhang, B. M. Weckhuysen and H. Su, Active sites over CuO/CeO<sub>2</sub> and inverse CeO<sub>2</sub>/CuO catalysts for preferential CO oxidation, *J. Power Sources*, 2014, **256**, 301–311.
  - 47 T. Xia, S. Yao, Z. Wu, G. Li and J. Li, High ratio of Ce<sup>3+</sup>/(Ce<sup>3+</sup>+Ce<sup>4+</sup>) enhanced the plasma catalytic degradation of n-undecane on CeO<sub>2</sub>/γ-Al<sub>2</sub>O<sub>3</sub>, *J. Hazard. Mater.*, 2022, **424**, 127700.
  - 48 R. Ma, Y. Zhou, C. Hu, M. Yang, F. Wang, K. Yan, Q. Liu and J. Wang, Post iron-doping of activated nitrogen-doped carbon spheres as a high-activity oxygen reduction electrocatalyst, *Energy Storage Mater.*, 2018, **13**, 142–150.
  - 49 Y. Ito, Y. Tanabe, J. Han, T. Fujita, K. Tanigaki and M. Chen, Multifunctional porous graphene for high-efficiency steam generation by heat localization, *Adv. Mater.*, 2015, **27**, 4302–4307.
  - 50 M. Hassan, E. Haque, K. R. Reddy, A. I. Minett, J. Chen and V. G. Gomes, Edge-enriched graphene quantum dots for enhanced photo-luminescence and supercapacitance, *Nanoscale*, 2014, **6**, 11988–11994.
  - 51 P. Sun, X. Wang, M. Zhu, N. Ahmad, K. Zhang and X. Xu, Nitrogen self-doped metal free catalysts derived from chitin via one step method for efficient electrocatalytic CO<sub>2</sub> reduction to CO, *Catalysts*, 2023, **13**, 904.
  - 52 C. Lu, Y. Chen, Y. Yang and X. Chen, Single-atom catalytic materials for lean-electrolyte ultrastable lithium-sulfur batteries, *Nano Lett.*, 2020, **20**, 5522–5530.
  - 53 L. Liu, S. Liu, L. Li, H. Qi, H. Yang, Y. Huang, Z. Wei, L. Li, J. Xu and B. Liu, A general method to construct single-atom catalysts supported on N-doped graphene for energy applications, *J. Mater. Chem. A*, 2020, **8**, 6190–6195.
  - 54 H. He, D. Huang, Y. Tang, Q. Wang, X. Ji, H. Wang and Z. Guo, Tuning nitrogen species in three-dimensional porous carbon via phosphorus doping for ultra-fast potassium storage, *Nano Energy*, 2019, **57**, 728–736.
  - 55 F. Khan, S.-H. Baek and J. H. Kim, One-step and controllable bipolar doping of reduced graphene oxide using TMAH as reducing agent and doping source for field effect transistors, *Carbon*, 2016, **100**, 608–616.
  - 56 F. Khan and J. H. Kim, Significance of N-moieties in regulating the electrochemical properties of nano-porous graphene: Toward highly capacitive energy storage devices, *J. Ind. Eng. Chem.*, 2018, **68**, 129–139.
  - 57 S. Xu, F. Xie, H. Xie, G. Zhou and X. Liu, Effect of structure and composition on the CO<sub>2</sub> hydrogenation properties over bimodal mesoporous CeCo composite catalyst, *Chem. Eng. J.*, 2019, **375**, 122023.
  - 58 B. Wei, J. Hao, B. Ge, W. Luo, Y. Chen, Y. Xiong, L. Li and W. Shi, Highly efficient electrochemical carbon dioxide reduction to syngas with tunable ratios over pyridinic-nitrogen rich ultrathin carbon nanosheets, *J. Colloid Interface Sci.*, 2022, **608**, 2650–2659.
  - 59 Y. Zhao, H. Wang, J. Li, Y. Fang, Y. Kang, T. Zhao and C. Zhao, Regulating the spin-state of rare-earth Ce single atom catalyst for boosted oxygen reduction in neutral medium, *Adv. Funct. Mater.*, 2023, **33**, 2305268.
  - 60 C. Liu, M. Zhang, H. Geng, P. Zhang, Z. Zheng, Y. Zhou and W. He, NIR enhanced peroxidase-like activity of Au@CeO<sub>2</sub> hybrid nanozyme by plasmon-induced hot electrons and photothermal effect for bacteria killing, *Appl. Catal., B*, 2021, **295**, 120317.
  - 61 Y. Mao, P. Wang, L. Li, Z. Chen, H. Wang, Y. Li and S. Zhan, Unravelling the Synergy between Oxygen Vacancies and Oxygen Substitution in BiO<sub>2-x</sub> for Efficient Molecular-Oxygen Activation, *Angew. Chem., Int. Ed.*, 2020, **59**, 3685–3690.
  - 62 B. Dai, S. Cao, H. Xie, G. Zhou and S. Chen, Reduction of CO<sub>2</sub> to CO via reverse water-gas shift reaction over CeO<sub>2</sub> catalyst, *Korean J. Chem. Eng.*, 2017, **35**, 421–427.
  - 63 J. Liu, G. Li, C. Xu, H. Chen, R. Jin, L. Sun, C. Shu, H. Chen, C. Guo, H. Li and Y. Si, Designing Ce single-atom-sites coupled with CeO<sub>2</sub> nanoparticles for oxygen reduction enhancement, *Inorg. Chem. Front.*, 2023, **10**, 3091–3102.
  - 64 Y. Liang, C. Wu, S. Meng, Z. Lu, R. Zhao, H. Wang, Z. Liu and J. Wang, Ag single atoms anchored on CeO<sub>2</sub> with interfacial oxygen vacancies for efficient CO<sub>2</sub> electroreduction, *ACS Appl. Mater. Interfaces*, 2023, **15**, 30262–30271.
  - 65 D. Gao, Y. Zhang, Z. Zhou, F. Cai, X. Zhao, W. Huang, Y. Li, J. Zhu, P. Liu, F. Yang, G. Wang and X. Bao, Enhancing CO<sub>2</sub> electroreduction with the metal-oxide interface, *J. Am. Chem. Soc.*, 2017, **139**, 5652–5655.
  - 66 Z. Geng, X. Kong, W. Chen, H. Su, Y. Liu, F. Cai, G. Wang and J. Zeng, Oxygen vacancies in ZnO nanosheets enhance CO<sub>2</sub> electrochemical reduction to CO, *Angew. Chem.*, 2018, **130**, 6162–6167.
  - 67 Y. Guan, S. Wu, H. Huang, Z. Zhu, W. Tian and A. Yin, Promotion of CO<sub>2</sub> electroreduction on bismuth nanosheets



- with cerium oxide nanoparticles, *Chem.-Asian J.*, 2024, e202400296.
- 68 X. Ren, Y. Gao, L. Zheng, Z. Wang, P. Wang, Z. Zheng, Y. Liu, H. Cheng, Y. Dai and B. Huang, Oxygen vacancy enhancing CO<sub>2</sub> electrochemical reduction to CO on Ce-doped ZnO catalysts, *Surface. Interfac.*, 2021, **23**, 100923.
- 69 Y. Du, F. Gao, Y. Zhou, H. Yi, X. Tang and Z. Qi, Recent advance of CuO-CeO<sub>2</sub> catalysts for catalytic elimination of CO and NO, *J. Environ. Chem. Eng.*, 2021, **9**, 106372.
- 70 Z. Hou, W. Pei, X. Zhang, K. Zhang, Y. Liu, J. Deng, L. Jing and H. Dai, Rare earth oxides and their supported noble metals in application of environmental catalysis, *J. Rare Earths*, 2020, **38**, 819–839.
- 71 J. Zhu and S. Mu, Defect engineering in carbon-based electrocatalysts: insight into intrinsic carbon defects, *Adv. Funct. Mater.*, 2020, **30**, 2001097.
- 72 C. Xie, D. Yan, W. Chen, Y. Zou, R. Chen, S. Zang, Y. Wang, X. Yao and S. Wang, Insight into the design of defect electrocatalysts: from electronic structure to adsorption energy, *Mater. Today*, 2019, **31**, 47–68.
- 73 Z. Z. Wu, P. P. Yang and M. R. Gao, Dynamic evolution of copper-based catalysts during CO<sub>2</sub> electroreduction, *Nano Mater. Sci.*, 2024, DOI: [10.1016/j.nanoms.2024.01.007](https://doi.org/10.1016/j.nanoms.2024.01.007).
- 74 D. Gao, Y. Zhang, Z. Zhou, F. Cai, X. Zhao, W. Huang, Y. Li, J. Zhu and P. Liu, Enhancing CO<sub>2</sub> electroreduction with the metal–oxide interface, *J. Am. Chem. Soc.*, 2017, **139**(16), 5652–5655.
- 75 J. Xue, X. Fu, S. Geng, K. Wang, Z. Li and M. Li, Boosting electrochemical CO<sub>2</sub> reduction via valence state and oxygen vacancy controllable Bi–Sn/CeO<sub>2</sub> nanorod, *J. Environ. Manage.*, 2023, **342**, 118354.
- 76 L. Liao, G. Xia, F. Yu, X. Liu, M. Shu, G. Zhang, X. Zeng and H. Wang, Saturated Coordination Lu–N<sub>6</sub> Defect Sites for Highly Efficient Electroreduction of CO<sub>2</sub>, *Small*, 2023, **19**, 2300926.
- 77 J. Mou, J. Hu, T. Chen, K. Wang, K. Wang, W. Zhang, S. Wu, J. Shi and P. Zhao, Oxygen vacancies on CuGa<sub>2</sub> catalysts enhance CO<sub>2</sub> reduction to CO, *Sustain. Energy Fuels*, 2024, **8**(23), 5428–5436.

